Title	Growth of 1T ' MoTe2 by thermally assisted conversion of electrodeposited tellurium films
Author(s)	Mc Manus, John B.; Cunningham, Graeme; McEvoy, Niall; Cullen, Conor P.; Gity, Farzan; Schmidt, Michael; McAteer, David; Mullarkey, Daragh; Shvets, Igor V.; Hurley, Paul K.; Hallam, Toby; Duesberg, Georg S.
Publication date	2018-12-05
Original citation	Mc Manus, J. B., Cunningham, G., McEvoy, N., Cullen, C. P., Gity, F., Schmidt, M., McAteer, D., Mullarkey, D., Shvets, I. V., Hurley, P. K., Hallam, T., Duesberg, G. S. (2019) 'Growth of 1T ' MoTe2 by Thermally Assisted Conversion of Electrodeposited Tellurium Films', ACS Applied Energy Materials, 2, pp. 521-530. doi: 10.1021/acsaem.8b01540
Type of publication	Article (peer-reviewed)
Link to publisher's version	https://pubs.acs.org/doi/10.1021/acsaem.8b01540 http://dx.doi.org/10.1021/acsaem.8b01540 Access to the full text of the published version may require a subscription.
Rights	© 2018 American Chemical Society. This article is made available for a limited time sponsored by ACS under the ACS Free to Read License, which permits copying and redistribution of the article for non-commercial scholarly purposes. https://pubs.acs.org/page/policy/freetoread/index.html
Item downloaded from	http://hdl.handle.net/10468/9782

University College Cork, Ireland
Coláiste na hOllscoile Corcaigh

Growth of 1T′ MoTe2 by Thermally Assisted Conversion of Electrodeposited Tellurium Films

John B. Mc Manus,[†,‡] Graeme Cunningham,[†,‡] Niall McEvoy,[†,‡] Conor P. Cullen,[†,‡] Farzan Gity,[§] Michael Schmidt,[§] David McAteer,[‡,∥] Daragh Mullarkey,[∥] Igor V. Shvets,[∥] Paul K. Hurley,[‡] Toby Hallam,*[,⊥] and Georg S. Duesberg*[,†,#]

[†]School of Chemistry, [‡]AMBER Centre, CRANN Institute, and [∥]School of Physics, Trinity College Dublin, Dublin 2, D02 PN40, Ireland

[§]Tyndall National Institute, University College Cork, Lee Maltings, Dyke Parade, Cork, T12 R5CP, Ireland

[⊥]Emerging Technologies and Materials Group, School of Engineering, Newcastle University, Merz Court, Newcastle Upon Tyne, NE1 7RU, United Kingdom

[#]Institute of Physics, EIT 2, Faculty of Electrical Engineering and Information Technology, Universität der Bundeswehr, 85579 Neubiberg, Germany

Ⓢ Supporting Information

ABSTRACT: Molybdenum ditelluride ($MoTe_2$) is a transition metal dichalcogenide (TMD) which has two phases stable under ambient conditions, a semiconducting (2H) and semimetallic (1T′) phase. Despite a host of interesting properties and potential applications, $MoTe_2$ is one of the less-studied TMDs, perhaps due its relatively low abundance in nature or challenges associated with its synthesis, such as the toxicity of most precursors. In this report, we describe the fabrication of thin films of phase-pure 1T′ $MoTe_2$ using predeposited molybdenum and electrodeposited tellurium layers, at the relatively low temperature of 450 °C. This method allows control over film geometry and over the tellurium concentration during the conversion. The $MoTe_2$ films are characterized by Raman spectroscopy, X-ray photoelectron spectroscopy, X-ray diffraction, atomic force microscopy, and electron microscopies. When applied as a catalyst for the hydrogen evolution reaction, the films display promising initial results. The $MoTe_2$ films have a Tafel slope of below 70 mV dec^{-1} and compare favorably with other $MoTe_2$ catalysts reported in the literature, especially considering the inherently scalable fabrication method. The variation in electrocatalytic behavior with thickness and morphology of the films is also investigated.

KEYWORDS: $MoTe_2$, 1T′ phase, thin-film, Raman spectroscopy, electrocatalysis, hydrogen evolution reaction
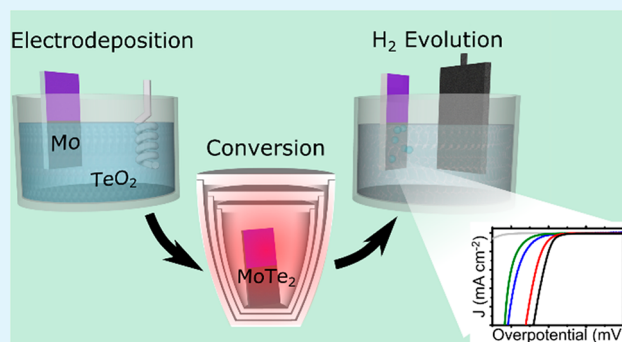
INTRODUCTION

Layered transition metal dichalcogenides (TMDs) have become one of the primary areas of focus for nanoscale materials research.[1,2] They display a diverse range of properties which has led to suggested applications in many areas of materials science such as electronics, optoelectronics, photonics, sensing, and catalysis.[3−6] While in general there has been exceptional progress in the research on TMDs, the focus thus far has primarily been on the Group VI TMDs containing sulfur or selenium. The equivalent telluride TMDs, $MoTe_2$ and WTe_2, have not been studied nearly as extensively, despite having some very exciting properties making their further investigation worthwhile.[7−11] This slower uptake may in part be due to the high toxicity of many of the tellurium precursors necessary for the growth of these films and difficulties in obtaining phase-pure growth of $MoTe_2$.[12] Additionally, the

telluride-containing TMDs are not naturally abundant, unlike MoS_2, meaning that synthesis is necessary.

Three structural phases of $MoTe_2$ have been studied: the 2H, trigonal prismatic phase; the 1T′ distorted-octahedral or monoclinic phase; and finally the T_d orthorhombic phase.[13] The semiconducting, 2H phase of $MoTe_2$ is the most thermodynamically stable, with a small ground-state energy difference between it and the semimetallic 1T′ phase of only 35 meV per formula unit.[12] This means that, at ambient conditions, both phases can be stable, opening up applications as a possible phase-change material for energy storage or sensors.[14] While presenting a fabrication challenge, this property may also offer a great opportunity to address the
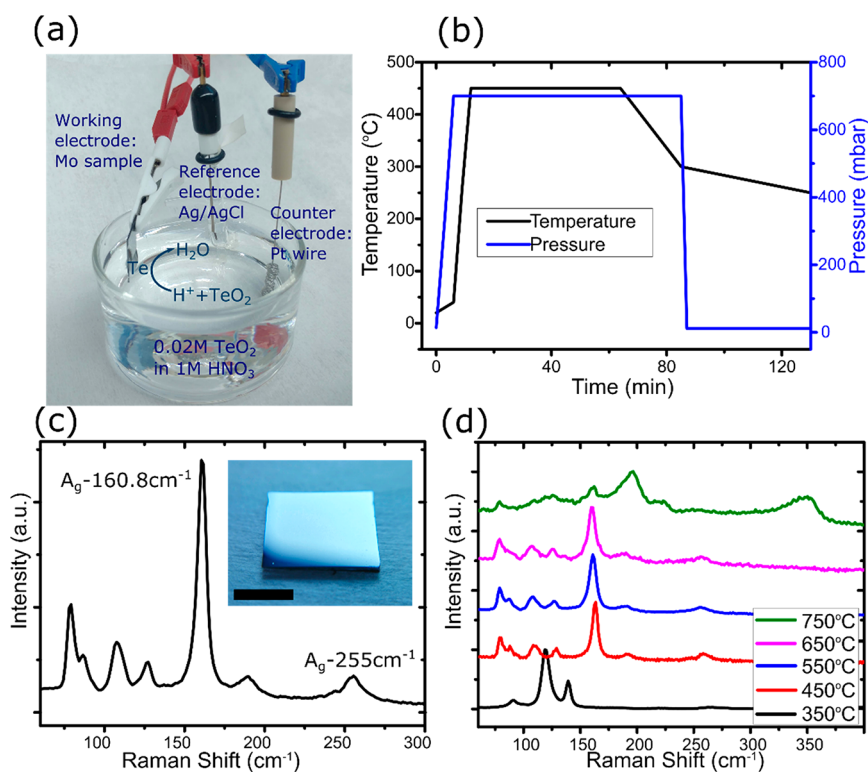
Figure 1. (a) Picture of the setup for electrodeposition of tellurium. The TeO_2 in solution is reduced onto the molybdenum metal film which acts as the working electrode in the setup. (b) Furnace temperature and pressure growth conditions for the $MoTe_2$ thin-films. (c) Main: Raman spectrum of a typical 20 nm $MoTe_2$ film showing the characteristic peaks expected from the 1T′ phase. Inset: Picture of the $MoTe_2$ film on SiO_2/Si wafer after conversion. Scale bar is 5 mm. (d) Raman spectra for a number of $MoTe_2$ films grown at different temperatures using this conversion method.

issue of contact resistance in semiconducting devices.[15] By creating 1T′:2H junctions in $MoTe_2$, it could be possible to create contacts to semiconducting 2H $MoTe_2$ with ultralow contact resistance.[16]

The 2H phase of $MoTe_2$ is a promising candidate for use in optoelectronics including visible and short-wave IR photodetection.[7,17,18] 1T′ $MoTe_2$ is a type-II Weyl semimetal and has demonstrated a number of other novel features such as giant magnetoresistance and pressure-sensitive superconductivity.[8−11] 1T′ $MoTe_2$ nanosheets have also shown promise as an electrode material for supercapacitors.[19] Due to their relatively high electrical conductivity and Seebeck coefficient, along with their low thermal conductivity, TMDs have attracted attention for their potential as high-performance thermoelectric materials.[20] The unique ability to grow stable, mixed-phase films of semiconducting 2H and the strongly anisotropic, semimetallic 1T′ $MoTe_2$ is an especially interesting prospect in this regard.[20] Due to these many and varied qualities, developing reliable fabrication methods for $MoTe_2$ is of immediate interest.

The majority of studies thus far have focused on using bulk single crystals or mechanically exfoliated flakes of $MoTe_2$ obtained from chemical vapor transport (CVT).[21−23] These offer relatively defect-free systems, enabling impressive proof-of-concept results; however, mechanical exfoliation is an inherently unscalable process and even the synthesis of $MoTe_2$ crystals by CVT is a lengthy and energy-intensive process.[22] There has recently been an increasing amount of work emerging on the growth of nanoscale $MoTe_2$ by more scalable methods, such as chemical vapor deposition (CVD). A number of groups have reported growth of monolayer crystals

with partial surface coverage,[24−30] while others have shown large-area coverage of few-layer films.[31−35] Despite this, reproducible synthesis of layer-controlled $MoTe_2$, over a defined area, is still in its infancy. This, along with inherent advantages for certain applications, leaves a strong case for the development of a straightforward growth method for large-scale, polycrystalline thin-films of $MoTe_2$. One way to produce these films is through thermally assisted conversion (TAC) of a predeposited metal film in a chalcogen atmosphere.[36,37] While not suitable for all applications, these films can be relevant for areas such as catalysis where under-coordinated sites at defects and along grain boundaries can act as efficient active sites.[38]

A major area of research for electrocatalysis is the efficient production of hydrogen through the hydrogen evolution reaction (HER). Realization of this would have a plethora of benefits including improved energy storage to complement renewable energy production. At present, one of the major challenges is that efficient hydrogen evolution requires expensive platinum-group catalysts.[39] Layered TMDs have been shown to be viable candidates for electrocatalytic applications, especially when in a (semi)metallic phase, due to their much higher conductivity.[40] Both MoS_2 and $MoSe_2$ have shown some particularly promising results in this regard,[41−44] while WTe_2 and $MoTe_2$ have also been investigated, with the 1T′ phase of $MoTe_2$ shown to be much more active than the semiconducting 2H phase.[45−47]

In this work nanoscale thin films of $MoTe_2$ are grown from a film of predeposited Mo. This growth allows for strong control of the thickness and spatial coverage of the $MoTe_2$. Unlike previously reported work, the Te is electrodeposited on top of

the Mo prior to furnace growth. This method allows for high precision in the quantity of Te present for the reaction, allaying any issues of furnace poisoning from excess Te and side products. The reaction takes place in an enclosed crucible in a quartz furnace at 450 °C, making this growth potentially compatible with silicon back-end-of-line processing. Indeed, this is one of the few TMD growth methods reported which can be achieved at this low temperature. The 1T′ phase $MoTe_2$ films are extensively characterized to reveal phase-pure conversion with low levels of oxide and large domain sizes. The large-area films show promising results for use as catalysts of the hydrogen evolution reaction with activity which trends with film thickness due to changing film morphology.

■ EXPERIMENTAL SECTION

$MoTe_2$ Film Growth. A film of Mo was deposited on a silicon wafer with 300 nm silicon oxide using a Temescal FC2000 electron-beam evaporation system. An initial Mo layer thickness of 20 nm was used throughout, unless otherwise stated. To electrodeposit Te from a solution of 0.02 M TeO_2 in 1 M nitric acid, the SiO_2/Si wafer with Mo acted as the working electrode in an electrochemical cell with a platinum counter electrode and a Ag/AgCl reference electrode, as pictured in Figure 1a. The pulsed Te deposition consisted of 10 ms pulses with 50 ms gaps, at −0.3 V with respect to the reference electrode and proceeded via the reaction:[48]

$$HTeO_2^+ + 3H^+ + 4e^- \rightarrow Te + 2H_2O$$
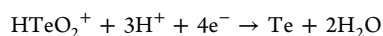
Typically 15,000 pulses of this duration were used. Pulsing of the potential offers better control of deposition properties such as morphology and uniformity of deposition.[48] Further detail is given in Figure S1 of the Supporting Information.

Following the Te deposition, the films were converted to $MoTe_2$ in an ATV PEO 604 quartz furnace at 450 °C. The reaction took place under nitrogen atmosphere at a pressure of ~700 mbar. The samples were placed inside nested crucibles in the furnace in order to have a high partial pressure of Te in the vicinity of the samples and to avoid contamination of the furnace (see Supporting Information, Figure S2). The temperature was ramped at 180 °C min^{-1} and held at the growth temperature for 55 min. The samples were then allowed to cool to near room temperature (<30 °C) under N_2 over a period of ~3 h before removal from the furnace. During the cooling, at ~320 °C, the pressure was lowered from ~700 mbar to 13 mbar. If the pressure was not lowered, there was found to be an increased likelihood of Te crystals remaining on the surface of the film. All samples are named by referring to the thickness of the starting Mo film.

Sample Characterization. A WITec Alpha 300R with a 532 nm excitation laser, with a power of ~200 μW, was used to collect the Raman spectra shown herein. All Raman measurements were taken using a spectral grating with 1800 lines/mm and a 100× objective lens. Raman spectra shown are averages of maps which were generated by taking scans every 400 nm in the x and y directions, typically over an area of 20 × 20 μm^2, making each spectrum an average of ~2500 spectra.

X-ray photoelectron spectroscopy (XPS) spectra were taken using monochromated Al Kα X-rays from an Omicron XM1000 MkII X-ray source and an Omicron EA125 energy analyzer. An Omicron CN10 electron flood gun was used for charge compensation. Core-level scans were recorded at an analyzer pass energy of 15 eV. Analysis was performed using CasaXPS software. Spectral components were fitted using a Shirley background subtraction and appropriate line shapes. Relative atomic percentages were calculated using the relative sensitivity factors provided by the software CasaXPS.

Scanning electron microscopy (SEM) images were obtained with a Karl Zeiss Supra microscope operating at 3 kV accelerating voltage, 30 μm aperture and a working distance of ~3–4 mm.

Transmission electron microscopy (TEM) analysis was performed using a JEOL JEM-2100 at 200 kV in bright field mode. Cross-

sectional TEM was prepared using a dual beam focused ion beam (FIB) FEI Helios NanoLab 600i. A 50 nm carbon layer which was followed by a 300 nm platinum layer were deposited within the dual beam FIB by electron beam induced deposition and a 2 μm thick carbon layer was then deposited by ion beam induced deposition. These three layers were deposited for protection before the milling process. The lamella was prepared and thinned down to less than 200 nm thickness.

Atomic force microscopy (AFM) was carried out on a Bruker Multimode 8 in ScanAsyst Air mode using Nanosensor PointProbe Plus tips.

The X-ray diffraction (XRD) measurement was performed on a Bruker D8 Discover with a monochromated Cu Kα source.

Electrochemical Measurements. The samples for electrochemical characterization were fabricated in a similar fashion to those described already; however, the Mo layer was evaporated on a pyrolytic carbon (PyC) layer which had been previously grown on the silicon wafer. The PyC was grown by CVD of acetylene at 950 °C for 30 min on 300 nm thermal SiO_2 on Si substrates in a hot-wall, quartz-tube furnace; full details can be found in the previous work by McEvoy et al.[49] The samples were all converted to $MoTe_2$ at 450 °C as described above.

The samples were measured in a three-electrode electrochemical cell with sulfuric acid (0.5 M) as the electrolyte with the $MoTe_2$ film as the working electrode, a large graphitic counter electrode, and a Ag/AgCl reference electrode. All potentials quoted are given as overpotential (OP); the measured potential was converted to overpotential using the formula $E_{OP} = E_{measured} + 0.2$ V. Catalytic activity was measured by performing linear sweep voltammetry (LSV) and electrochemical impedance spectroscopy (EIS) with either a Gamry Reference 3000 or 600 potentiostat at an overpotential of 0 mV. Sample conditioning was performed prior to each test. Linear voltage sweeps were performed at a scan rate of 5 mV s^{-1} in a voltage range −0.2 V to −1.2 V (vs Ag/AgCl). EIS in the frequency range of 0.1 to 10 MHz with perturbation voltage amplitude of 10 mV was used to determine the equivalent series resistance of the system. All the data was corrected for the electrolyte resistance by iR compensation.

Chronoamperometry was carried out using the same experimental setup with a fixed potential applied for a period of time and the current response measured. This data was not iR compensated.

■ RESULTS AND DISCUSSION

The fabrication of $MoTe_2$ thin-films was carried out in an enclosed crucible by the reaction of predeposited Mo metal films with electrodeposited Te. Electrodeposition was used as a method of spatially controlling and directing the Te deposition on each sample. This deposition method allowed a very small, yet well-defined, amount of Te to be used in the reaction. It ensured that the deposited Te was always located directly in contact with the Mo allowing for high local Te concentrations during conversion but avoided the requirement for excessive amounts of toxic Te, as in the case of evaporation, which could result in furnace poisoning. Figure 1b shows the temperature and pressure values throughout the conversion to $MoTe_2$.

An image of a converted film in shown in Figure 1c inset. The films show good optical uniformity over the sample with the film's lateral dimensions limited only by the furnace size. This method easily allows for the fabrication of films of varying thickness; here samples which had an initial 20 nm of Mo deposited were used for characterization. A typical Raman spectrum of such a sample is shown in Figure 1c. The peaks visible are consistent with previously published spectra of 1T′ $MoTe_2$ and confirm the successful conversion to the TMD using this method.[50,51] 1T′ $MoTe_2$ is a member of the $P2_1/m$ space group (C_{2h}^2 point group); due to this low symmetry it has a large number of Raman-active modes, the most

prominent here being the A_g peak at 160.9 cm^{-1}.[27] The peaks at 79, 86.8, 126.8, 160.9, and 255 cm^{-1} each have the symmetry A_g, while the ones at ~108 cm^{-1} and ~190 cm^{-1} are B_g. Fitting and labeling of all peaks is shown in Figure S3 of the Supporting Information. The peak at 160.9 cm^{-1} has been referred to as both A_g and B_g symmetry in the literature, with the earliest assignment of these symmetries we have found to be the work of Ma et al.[50] and Keum et al.,[8] respectively. Taking into account the studies done by Ma et al. and Song et al.,[51] where they calculated the 1T′ MoTe$_2$ peak symmetries and confirmed their predictions using polarized Raman spectroscopy, in this paper we have referred to the peak as A_g.

There is no indication of residual Te present in the Raman spectra of films obtained from our typical growth process; however, if the growth time is reduced, or the initial layer thickness of Te is substantially increased, both MoTe$_2$ and TeO$_2$ are visible in the Raman spectra, as shown in Figure S4 of the Supporting Information. This likely stems from the presence of unreacted Te which then oxidized when exposed to atmosphere.

Raman spectroscopy was further used to examine the temperature range in which MoTe$_2$ could be grown. Figure 1d shows the Raman spectra of a series of MoTe$_2$ films grown at different temperatures between 350 and 750 °C. Below 450 °C there is no evidence of MoTe$_2$ and the Raman analysis reveals a spectrum identical to that of the predeposited Te film, with only TeO$_2$ peaks visible. This may be due to the Te not melting as its melting point is ~450 °C at standard pressure, which is close to the growth pressure (~700 mbar) used here. Between 450 °C and 650 °C there is consistent conversion to 1T′ MoTe$_2$ with very similar Raman spectra. It is worth noting that this conversion temperature is lower than most other reports for MoTe$_2$, particularly for the 1T′ phase which typically requires high temperatures for growth and a quenching cool to prevent reversion to the 2H phase.[31,33,52] There may be a number of reasons for our observation of low-temperature growth, including that the 1T′ phase is reportedly stabilized on metallic substrates, or that the polycrystalline nature of these films serves to stabilize the 1T′ phase. The small electronegativity difference between Mo and Te can lead to higher incidences of Te vacancies and it has been previously suggested that the 1T′ phase is stabilized by these Te vacancies.[16] Above 650 °C the film conversion was inconsistent with a large amount of molybdenum oxides and some 1T′ MoTe$_2$ signal present.[53] The growth of the 2H phase of MoTe$_2$ was not observed at any temperature despite this being the most stable phase. This may be due to the factors discussed above. Furthermore, it has also been reported that strain or tellurium deficiency can influence MoTe$_2$ phase.[12,34]

XPS analysis of the MoTe$_2$ films confirmed the conversion of the films to MoTe$_2$. Figure 2a,b show the fitted peaks in the Mo 3d and the Te 3d core-level regions from a typical MoTe$_2$ film. The Mo 3d core-level displays a doublet associated with MoTe$_2$ at a binding energy (BE) of 227.7 eV and a small component from molybdenum oxide at 233.2 eV. The Te 3d core-levels associated with MoTe$_2$ and TeO$_2$ are at BE of 572.2 and 576 eV, respectively. The asymmetric shape of the components corresponding to MoTe$_2$ indicates the metallic nature of the material, further confirming that it is the 1T′ phase of MoTe$_2$. The calculated stoichiometry from XPS is MoTe$_{1.8}$. While there is some level of error associated with the stoichiometry ratio from XPS, this tellurium deficiency in the
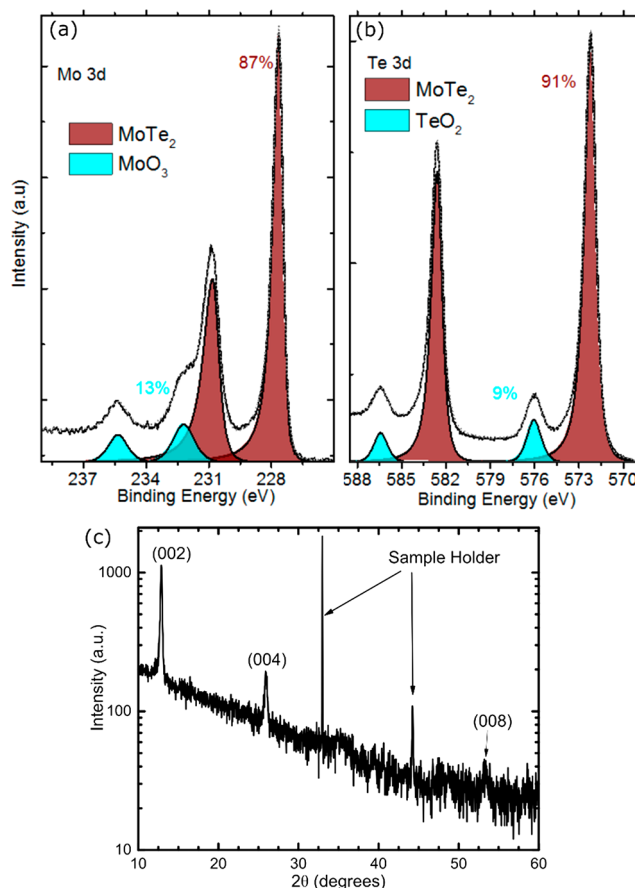

Figure 2. (a) Mo 3d XPS spectrum showing the percentage of Mo atoms in the sample bound to either oxygen as MoO$_3$ or tellurium as MoTe$_2$. (b) Te 3d spectral region showing the percentage of TeO$_2$ present in the sample (c) XRD spectrum of MoTe$_2$ thin film which shows the (002), (004), and (008) peaks. This is quite noisy due to the rough polycrystalline nature of the films.

material may explain the selective growth of the 1T′ phase rather than 2H MoTe$_2$.

Oxide components are present for both Mo and Te in the form of MoO$_3$ and TeO$_2$ as the samples were exposed to atmosphere between growth and characterization. Of the Mo atoms ~13% are in an oxide, while for the Te it is ~9%. TMD tellurides are known to more readily oxidized than other TMDs, especially if the films are polycrystalline.[21,54] It is likely that the oxidation process is self-limiting; as such, it is expected that analysis of the bulk would show less oxide.[55]

The conversion of the film to 1T′ MoTe$_2$ was further confirmed by XRD as shown in Figure 2c. The spectrum measured is consistent with previously reported XRD of 1T′ MoTe$_2$.[56] Two peaks from the sample holder are also labeled in the spectrum.

The morphology of the MoTe$_2$ films was analyzed using electron microscopies. In Figure 3a an SEM image of the flake-like morphology of the MoTe$_2$ film after conversion is shown. This is very different from the hexagonal rod morphology seen in the electrodeposited Te prior to conversion shown in Figure S5 of the Supporting Information. From this figure it is also clear that the 15,000 pulse electrodeposition gives a Te film thickness of 200−250 nm. The converted MoTe$_2$ film's crystal sizes are on the order of hundreds of nanometers and many protrude at a high angle to the surface. This is further
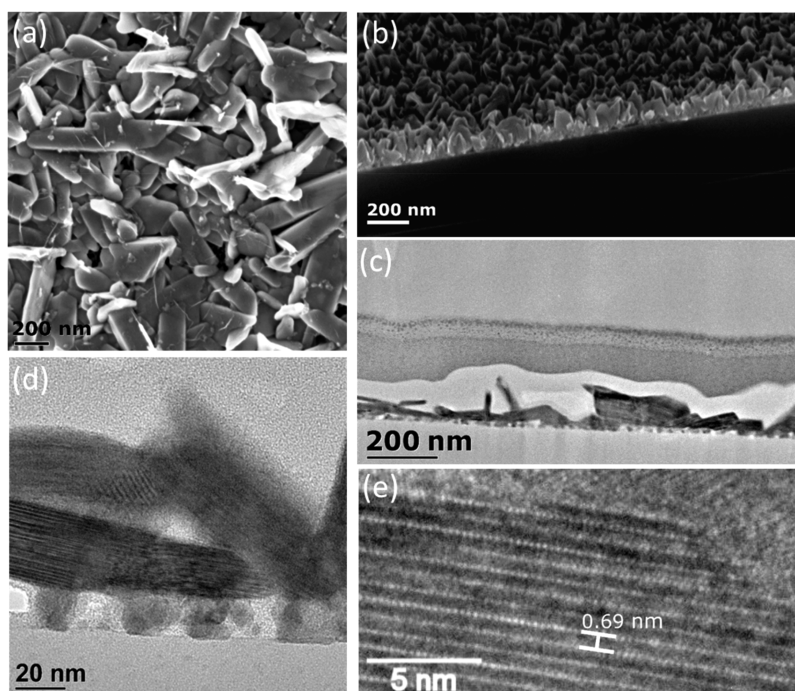
Figure 3. (a) SEM of 20 nm MoTe$_2$ film showing the rough, flake-like nature of the films. (b) SEM image of a cleaved SiO$_2$/Si wafer with MoTe$_2$ growth on top. This gives a good representation of the vertical alignment of the crystal growth (c) and (d) TEM cross section of MoTe$_2$ film. The crystalline flakes are visible along with the amorphous sublayer. (e) TEM image of a crystal showing the layer separation of the MoTe$_2$.

demonstrated by the "cross-section" view of a cleaved silicon wafer and MoTe$_2$ film in Figure 3b. The vertical nature of the flakes is similar to the previously reported edge-growth of MoS$_2$ films, though in this case the crystals are less aligned.[43]

Thinned lamellas were prepared for use in cross-sectional TEM. Figure 3c−e shows the randomly aligned nature of the domains in the film, along with the rough nature of the film surface. Examining the layers within a crystal shows an average separation of 0.69 nm which is consistent with the expected layer separation of MoTe$_2$ of ~0.7 nm.[56]

While the method used to grow the MoTe$_2$ films here can be considered an extension of previous work on the thermally assisted conversion of metallic films to TMDs, the nature of the reaction interface in this case is quite different. The majority of TAC work to date refer to solid films which are converted through exposure to vapor-phase chalcogens.[36,37,57] In this work, the reaction is occurring at a solid−liquid interface which results in a much higher chalcogen concentration at the interface. This is expected to be a large part of the reason for the quite different morphology—much larger crystal sizes and more out-of-plane nature of these crystals.

The proposed growth mechanism is that upon heating the Te begins to melt and diffuse into the Mo layer. This forms an intermixed layer of Mo and Te from which the MoTe$_2$ crystals nucleate and grow in a manner analogous to the solution−liquid−solid growth mechanism.[58] It is further proposed that, as the Te melts, it tends to dewet from the surface and form droplets on the surface. These droplets serve as areas of especially high Te concentration which then allow for much larger MoTe$_2$ crystals to form, as can be seen in Figure S6 in the Supporting Information. This mechanism is quite similar to that described by Kwak et al. in their growth of WTe$_2$ nanobelts; however, they used a layer of Cu on the surface with which vaporized Te formed a eutectic alloy before

reacting with the W.[59] The work presented here offers a simpler solution as it does not require a postgrowth etch to remove CuTe$_x$ residue.

It is evident from Figure 3d that below the crystalline MoTe$_2$ flakes there is an amorphous layer ~15−20 nm thick with some voids present. It is not clear what caused the formation of two distinct layers in the sample; one possibility is that the MoTe$_2$ crystals grow from the surface of the intermixed Mo−Te layer drawing material upward resulting in void formation. Supporting this hypothesis is the amorphous layer thickness being similar to, or slightly less than, the starting Mo layer (20 nm). Moreover, when this interfacial layer between the SiO$_2$ and the MoTe$_2$ crystals was probed using energy-dispersive X-ray spectroscopy (EDX) (Figure S7) there was evidence of a Te signal from throughout the sample.

TMDs have been shown to have strong electrocatalytic behavior and the MoTe$_2$ films grown here possess many promising characteristics in this regard.[60] As they are in the 1T′ phase, they have high conductivity which facilitates improved charge transport to the active sites.[40,61] Furthermore, it has been suggested for other TMDs, such as MoS$_2$, that in the 1T phase the basal plane becomes catalytically active.[62] Finally, due to these films' polycrystalline nature and vertically oriented flakes, there are expected to be a high number of under-coordinated and edge sites, both of which have been shown to improve catalytic behavior.[43,63,64] To demonstrate the applicability of these films, their performance as a catalyst for the hydrogen evolution reaction was examined. In this case, the MoTe$_2$ was grown on PyC which provides an ideal inert, conductive current collector due to its low reactivity and stability at high temperatures. This system of films on PyC has previously been used for the characterization of other TMDs such as MoS$_2$.[65,66] No substantive differences were observed in the films when grown on PyC rather than SiO$_2$/Si;
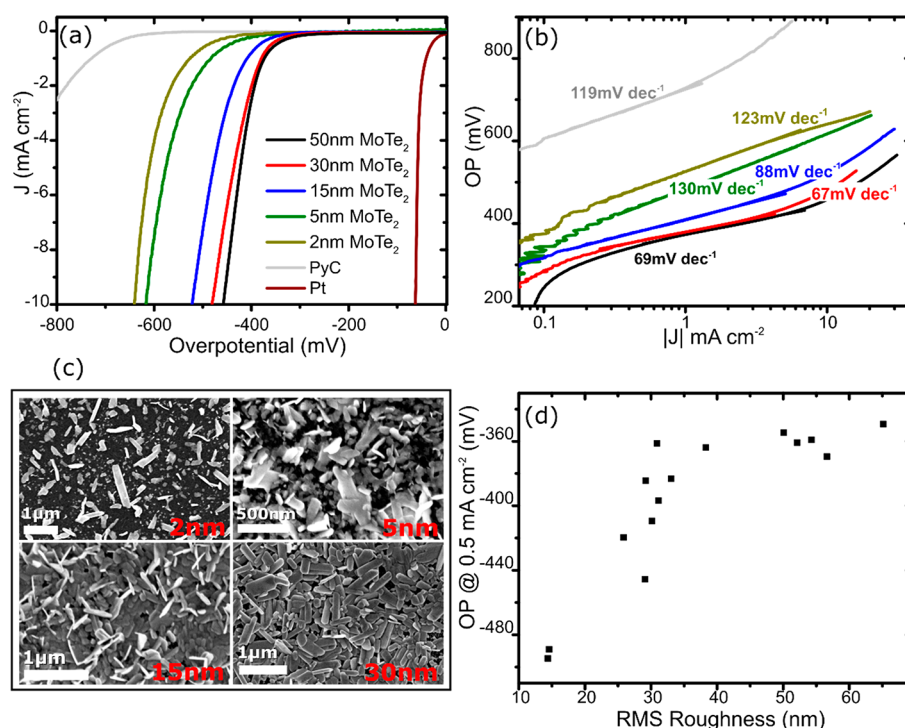
Figure 4. (a) Linear sweep voltammetry of MoTe$_2$ films of different thicknesses. All thicknesses refer to the starting Mo layer thickness. Also shown is the response of bare PyC and a 30 nm Pt film. (b) Corresponding Tafel plots with fitted slopes of the same samples. (c) SEM images of MoTe$_2$ samples of four different thickness showing the changing morphology. (d) Plot of the onset potential (overpotential (OP) required to measure 0.5 mA cm^{-2} of current density) versus the RMS roughness of the films. The onset potential drops noticeably before changing much more slowly with roughness above ~35 nm.

characterization of the MoTe$_2$ on PyC is shown in Figure S8 of the Supporting Information.

The catalytic performance of the MoTe$_2$ samples for HER was measured in a 0.5 M H$_2$SO$_4$ acidic cell with a graphite counter electrode. The results of the linear sweep voltammetry for representative films of different thickness can be seen in Figure 4a. From this, it is possible to extract the onset potential of the different films, defined here as the overpotential required to measure a current density of 0.5 mA cm^{-2}. It is evident that the thickness of the films has a strong influence on their effectiveness as catalysts for HER with the thicker films demonstrating markedly better behavior. Examining first the 50 nm MoTe$_2$ film, which is the best performing of the thicknesses examined here, it can be seen that it has an onset potential of 349 mV. While this is high compared to state-of-the art Pt catalysts (a 30 nm film of Pt on PyC measured here has an onset potential of ~30 mA), it is similar to the values for other relatively large-area MoTe$_2$ electrodes reported in the literature.[45,67] Comparisons of the films described herein to other published literature can be found in Table S1 in the Supporting Information.

The stability of these films was examined using chronoamperometry. A constant voltage of −0.6 V, with respect to the Ag/AgCl reference electrode, was applied to a sample and the current measured over a period of 190 min. The results are shown in Figure S9 of the Supporting Information. The film showed a 40% drop in current density over the applied time period which may be due to mechanical damage caused to the electrode by H$_2$ bubble formation.[65]

By plotting the log of the current density versus the overpotential, the Tafel plot is obtained, as shown in Figure 4b. Taking the slope of the linear region gives the Tafel slope,

which is related to the kinetics of the reaction steps involved in the evolution of hydrogen. Hydrogen evolution in acid can proceed by either the Volmer−Tafel or Volmer−Heyrovsky mechanisms. The Volmer reaction step is the electrochemical reduction of a proton in solution and adsorption of an intermediate hydrogen atom. If this is the rate-determining step, then a Tafel slope of 120 mV dec^{-1} is expected. Desorption of H$_2$ from the surface then occurs via either the Heyrovsky or the Tafel reaction. If the Heyrovsky step is rate determining, a slope of 40 to 120 mV dec^{-1} is anticipated, depending on surface coverage.[68] The Tafel reaction exhibits a slope of ~30 mV dec^{-1}. For applications such as HER it is generally accepted that a lower Tafel slope is desirable, as it can be understood to be the voltage increase required to increase the current density, and so hydrogen produced, by 1 order of magnitude.

Tafel slope values for each film thickness are shown in Figure 4b. The 30 and 50 nm films give the best performance by this metric with values below 70 mV dec^{-1}. These comparatively low values indicate that after the onset potential the current increases quite quickly leading to more competitive behavior at higher currents. These values compare very favorably with the Tafel slopes of MoTe$_2$ reported in the literature for the hydrogen evolution reaction. Films of liquid-exfoliated flakes have shown Tafel slopes of ~100 mV dec^{-1}.[42] Seok et al. examined single crystals of 1T′ MoTe$_2$, while McGlynn et al. looked at inkjet deposited MoTe$_2$ films; these reports showed Tafel slopes of 127 and 78 mV dec^{-1}, respectively.[45,69] Furthermore, both of these were smaller scale electrodes and, unlike this work, were not grown directly on the current collector. This system of TMD on PyC offers a cheaper, more scalable alternative to platinum-group catalysts.

In Figure 4a,b, the response of a bare PyC film can also be seen; clearly, this would have a negligible effect on the measurements due to its very low electrocatalytic activity in the measurement window.

It is evident from Figure 4a that the thickness of the films has a strong influence on their effectiveness as catalysts for HER; there is a much later onset of the reaction for the thinner films, with the 2 nm film having the highest OP before any measurable current is seen. In a similar way, the thicker films have a lower Tafel slope than the thinner (2 and 5 nm) films, with values on the order of 120 mV dec^{-1}, indicating that it is likely the Volmer reaction step which is rate limiting in the latter.

Further insight into this behavior can be gleaned by examining the morphologies of the films. The SEM images in Figure 4c show the noticeable differences between the films of different thicknesses. To quantify this, AFM was carried out on the films and the RMS roughness of each extracted. It was found that the roughness of the films increases with increasing thickness (Figure S10). The extracted roughness was then plotted against the respective onset potential (OP needed to measure 0.5 mA cm^{-2}) of each film (Figure 4d). There is a clear trend that initially the onset potential drops quickly as roughness increases, while above ∼35 nm the onset potential changes much more slowly. We expect that the decrease in onset potential correlates with roughness because a higher roughness indicates a more porous surface. This gives a greater effective surface area and so more active sites for the reaction to proceed. This increased porosity also offers improved access to the available active sites along with a reduction in mass transport limitations.

Not all surface information is captured by the roughness, however; as the films change morphology it could also be expected that there is change in the type of surface sites exposed, e.g., varying numbers of defects, or edge or basal plane sites due to the changing crystal sizes and orientation. We suggest that this is what is causing the rate at which the onset potential changes with roughness to vary over our measurement window. Further experiments, examining the type and density of active sites, would be needed to confirm this. As is, we have found that electrocatalytic behavior improves with increasing thickness of the MoTe$_2$ films up to a roughness of ∼35 nm, correlating to films with an initial starting Mo thickness of 20−30 nm. Increasing thickness beyond this does not show significant improvements in performance.

The described method allows for growth of large-area MoTe$_2$ films directly on inert, conductive PyC substrates without further processing. While not challenging the performance of Pt-based catalysts, they show encouraging HER results and, due to their nature, offer inherent scalability. This scalability is a valuable characteristic not encompassed by metrics such as the current density.

CONCLUSIONS

In this report we have demonstrated an efficient way to produce large-area thin films of 1T′ MoTe$_2$ by conversion of predeposited Mo and electrodeposited Te films. This method affords a high level of precision in local reactant concentration and so avoids potential issues with reactant handling and furnace poisoning. It is not specific to MoTe$_2$ and has the potential to produce numerous different TMD films in a reliable and scalable manner.

The growth of 1T′ MoTe$_2$ was successful at temperatures as low as 450 °C, which is of particular interest given the high temperatures required in other synthesis routes. This lowers the thermal budget of the synthesis and would allow the use of substrates such as aluminum, glass, and polyimide. Furthermore, it allows for potential back-end-of-line integration with silicon-based chips which is limited to 450 °C.

The films were characterized with Raman spectroscopy, XRD and XPS, with all indicating the presence of phase pure 1T′ MoTe$_2$. Application of the films as catalysts for the hydrogen evolution reaction produced promising results with the reported Tafel slope of below 70 mV dec^{-1} comparing well with previously reported literature. Additionally, it was found that thicker films have increasingly competitive behavior due to increased roughness.

ASSOCIATED CONTENT

Ⓢ Supporting Information

The Supporting Information is available free of charge on the ACS Publications website at DOI: 10.1021/acsaem.8b01540.

Diagram of electrodeposition; SEM images of Te film; Diagram of furnace; Labeled Raman spectra of MoTe$_2$ films; SEM images of Te and MoTe$_2$ surfaces; EDX elemental map of TEM cross-section; Raman of different thickness MoTe$_2$; Table of published HER results for MoTe$_2$; Electrochemical stability of films; AFM of MoTe$_2$ films (PDF)

AUTHOR INFORMATION

Corresponding Authors
*E-mail: Toby.Hallam@newcastle.ac.uk.
*E-mail: duesberg@unibw.de.
ORCID ⓘ
Farzan Gity: 0000-0003-3128-1426
Georg S. Duesberg: 0000-0002-7412-700X

Author Contributions

The manuscript was written through contributions of all authors. All authors have given approval to the final version of the manuscript.

Notes

The authors declare no competing financial interest.

ACKNOWLEDGMENTS

REFERENCES

(1) Bhimanapati, G. R.; Lin, Z.; Meunier, V.; Jung, Y.; Cha, J.; Das, S.; Xiao, D.; Son, Y.; Strano, M. S.; Cooper, V. R.; Liang, L.; Louie, S. G.; Ringe, E.; Zhou, W.; Kim, S. S.; Naik, R. R.; Sumpter, B. G.; Terrones, H.; Xia, F.; Wang, Y.; Zhu, J.; Akinwande, D.; Alem, N.; Schuller, J. A.; Schaak, R. E.; Terrones, M.; Robinson, J. A. Recent Advances in Two-Dimensional Materials beyond Graphene. *ACS Nano* **2015**, *9* (12), 11509−11539.

(2) Jariwala, D.; Sangwan, V. K.; Lauhon, L. J.; Marks, T. J.; Hersam, M. C. Emerging Device Applications for Semiconducting Two-Dimensional Transition Metal Dichalcogenides. *ACS Nano* **2014**, *8* (2), 1102−1120.

(3) Wang, H.; Feng, H.; Li, J. Graphene and Graphene-like Layered Transition Metal Dichalcogenides in Energy Conversion and Storage. *Small* **2014**, *10* (11), 2165−2181.

(4) Tan, C.; Cao, X.; Wu, X.-J.; He, Q.; Yang, J.; Zhang, X.; Chen, J.; Zhao, W.; Han, S.; Nam, G.-H.; Sindoro, M.; Zhang, H. Recent Advances in Ultrathin Two-Dimensional Nanomaterials. *Chem. Rev.* **2017**, *117* (9), 6225−6331.

(5) Tao, H.; Gao, Y.; Talreja, N.; Guo, F.; Texter, J.; Yan, C.; Sun, Z. Two-dimensional nanosheets for electrocatalysis in energy generation and conversion. *J. Mater. Chem. A* **2017**, *5* (16), 7257−7284.

(6) Gong, C.; Yuxi, Z.; Wei, C.; Junwei, C.; Tianyu, L.; Junru, P.; Liping, D.; Chunyang, W.; Yuhua, C.; Tianyou, Z.; Liang, L.; Jie, X. Electronic and Optoelectronic Applications Based on 2D Novel Anisotropic Transition Metal Dichalcogenides. *Advanced Science* **2017**, *4* (12), 1700231.

(7) Chen, Y.; Wang, X.; Wu, G.; Wang, Z.; Fang, H.; Lin, T.; Sun, S.; Shen, H.; Hu, W.; Wang, J.; Sun, J.; Meng, X.; Chu, J. High-Performance Photovoltaic Detector Based on MoTe$_2$/MoS$_2$ Van der Waals Heterostructure. *Small* **2018**, *14* (9), 1703293.

(8) Keum, D. H.; Cho, S.; Kim, J. H.; Choe, D.-H.; Sung, H.-J.; Kan, M.; Kang, H.; Hwang, J.-Y.; Kim, S. W.; Yang, H.; Chang, K. J.; Lee, Y. H. Bandgap opening in few-layered monoclinic MoTe$_2$. *Nat. Phys.* **2015**, *11*, 482.

(9) Chen, F. C.; Lv, H. Y.; Luo, X.; Lu, W. J.; Pei, Q. L.; Lin, G. T.; Han, Y. Y.; Zhu, X. B.; Song, W. H.; Sun, Y. P. Extremely large magnetoresistance in the type-II Weyl semimetal MoTe$_2$. *Phys. Rev. B: Condens. Matter Mater. Phys.* **2016**, *94* (23), 235154.

(10) Qi, Y.; Naumov, P. G.; Ali, M. N.; Rajamathi, C. R.; Schnelle, W.; Barkalov, O.; Hanfland, M.; Wu, S.-C.; Shekhar, C.; Sun, Y.; Süß, V.; Schmidt, M.; Schwarz, U.; Pippel, E.; Werner, P.; Hillebrand, R.; Förster, T.; Kampert, E.; Parkin, S.; Cava, R. J.; Felser, C.; Yan, B.; Medvedev, S. A. Superconductivity in Weyl semimetal candidate MoTe$_2$. *Nat. Commun.* **2016**, *7*, 11038.

(11) Berger, A. N.; Andrade, E.; Kerelsky, A.; Edelberg, D.; Li, J.; Wang, Z.; Zhang, L.; Kim, J.; Zaki, N.; Avila, J.; Chen, C.; Asensio, M. C.; Cheong, S.-W.; Bernevig, B. A.; Pasupathy, A. N. Temperature-driven topological transition in 1T′-MoTe$_2$. *npj Quantum Materials* **2018**, *3* (1), 2.

(12) Duerloo, K.-A. N.; Li, Y.; Reed, E. J. Structural phase transitions in two-dimensional Mo- and W-dichalcogenide monolayers. *Nat. Commun.* **2014**, *5*, 4214.

(13) Brown, B. E. The crystal structures of WTe$_2$ and high-temperature MoTe$_2$. *Acta Crystallogr.* **1966**, *20* (2), 268−274.

(14) Li, Y.; Duerloo, K.-A. N.; Wauson, K.; Reed, E. J. Structural semiconductor-to-semimetal phase transition in two-dimensional materials induced by electrostatic gating. *Nat. Commun.* **2016**, *7*, 10671.

(15) Chuang, H.-J.; Chamlagain, B.; Koehler, M.; Perera, M. M.; Yan, J.; Mandrus, D.; Tománek, D.; Zhou, Z. Low-Resistance 2D/2D Ohmic Contacts: A Universal Approach to High-Performance WSe$_2$, MoS$_2$, and MoSe$_2$ Transistors. *Nano Lett.* **2016**, *16* (3), 1896−1902.

(16) Cho, S.; Kim, S.; Kim, J. H.; Zhao, J.; Seok, J.; Keum, D. H.; Baik, J.; Choe, D.-H.; Chang, K. J.; Suenaga, K.; Kim, S. W.; Lee, Y. H.; Yang, H. Phase patterning for ohmic homojunction contact in MoTe$_2$. *Science* **2015**, *349* (6248), 625−628.

(17) Huang, H.; Jianlu, W.; Weida, H.; Lei, L.; Peng, W.; Xudong, W.; Fan, G.; Yan, C.; Guangjian, W.; Wenjin, L.; Hong, S.; Tie, L.; Jinglan, S.; Xiangjian, M.; Xiaoshuang, C.; Junhao, C. Highly sensitive visible to infrared MoTe$_2$ photodetectors enhanced by the photogating effect. *Nanotechnology* **2016**, *27* (44), 445201.

(18) Kuiri, M.; Chakraborty, B.; Paul, A.; Das, S.; Sood, A. K.; Das, A. Enhancing photoresponsivity using MoTe$_2$-graphene vertical heterostructures. *Appl. Phys. Lett.* **2016**, *108* (6), 063506.

(19) Liu, M.; Wang, Z.; Liu, J.; Wei, G.; Du, J.; Li, Y.; An, C.; Zhang, J. Synthesis of few-layer 1T′-MoTe$_2$ ultrathin nanosheets for high-performance pseudocapacitors. *J. Mater. Chem. A* **2017**, *5* (3), 1035−1042.

(20) Zhang, G.; Zhang, Y.-W. Thermoelectric properties of two-dimensional transition metal dichalcogenides. *J. Mater. Chem. C* **2017**, *5* (31), 7684−7698.

(21) Chen, B.; Sahin, H.; Suslu, A.; Ding, L.; Bertoni, M. I.; Peeters, F. M.; Tongay, S. Environmental Changes in MoTe$_2$ Excitonic Dynamics by Defects-Activated Molecular Interaction. *ACS Nano* **2015**, *9* (5), 5326−5332.

(22) Pradhan, N. R.; Rhodes, D.; Feng, S.; Xin, Y.; Memaran, S.; Moon, B.-H.; Terrones, H.; Terrones, M.; Balicas, L. Field-Effect Transistors Based on Few-Layered α-MoTe$_2$. *ACS Nano* **2014**, *8* (6), 5911−5920.

(23) Wang, B.; Yang, S.; Wang, C.; Wu, M.; Huang, L.; Liu, Q.; Jiang, C. Enhanced current rectification and self-powered photo-response in multilayer p-MoTe$_2$/n-MoS$_2$ van der Waals hetero-junctions. *Nanoscale* **2017**, *9* (30), 10733−10740.

(24) Apte, A.; Krishnamoorthy, A.; Hachtel, J. A.; Susarla, S.; Idrobo, J. C.; Nakano, A.; Kalia, R. K.; Vashishta, P.; Tiwary, C. S.; Ajayan, P. M. Telluride-Based Atomically Thin Layers of Ternary Two-Dimensional Transition Metal Dichalcogenide Alloys. *Chem. Mater.* **2018**, *30* (20), 7262−7268.

(25) Naylor, C. H.; Parkin, W. M.; Ping, J.; Gao, Z.; Zhou, Y. R.; Kim, Y.; Streller, F.; Carpick, R. W.; Rappe, A. M.; Drndić, M.; Kikkawa, J. M.; Johnson, A. T. C. Monolayer Single-Crystal 1T′-MoTe$_2$ Grown by Chemical Vapor Deposition Exhibits Weak Antilocalization Effect. *Nano Lett.* **2016**, *16* (7), 4297−4304.

(26) Ding, Y.; Zhou, N.; Gan, L.; Yan, X.; Wu, R.; Abidi, I. H.; Waleed, A.; Pan, J.; Ou, X.; Zhang, Q.; Zhuang, M.; Wang, P.; Pan, X.; Fan, Z.; Zhai, T.; Luo, Z. Stacking-mode confined growth of 2H-MoTe$_2$/MoS$_2$ bilayer heterostructures for UV−vis−IR photodetectors. *Nano Energy* **2018**, *49*, 200−208.

(27) Empante, T. A.; Zhou, Y.; Klee, V.; Nguyen, A. E.; Lu, I. H.; Valentin, M. D.; Naghibi Alvillar, S. A.; Preciado, E.; Berges, A. J.; Merida, C. S.; Gomez, M.; Bobek, S.; Isarraraz, M.; Reed, E. J.; Bartels, L. Chemical Vapor Deposition Growth of Few-Layer MoTe$_2$ in the 2H, 1T′, and 1T Phases: Tunable Properties of MoTe$_2$ Films. *ACS Nano* **2017**, *11* (1), 900−905.

(28) Sung, J. H.; Heo, H.; Si, S.; Kim, Y. H.; Noh, H. R.; Song, K.; Kim, J.; Lee, C.-S.; Seo, S.-Y.; Kim, D.-H.; Kim, H. K.; Yeom, H. W.; Kim, T.-H.; Choi, S.-Y.; Kim, J. S.; Jo, M.-H. Coplanar semiconductor−metal circuitry defined on few-layer MoTe$_2$ via polymorphic heteroepitaxy. *Nat. Nanotechnol.* **2017**, *12*, 1064.

(29) Zhou, J.; Liu, F.; Lin, J.; Huang, X.; Xia, J.; Zhang, B.; Zeng, Q.; Wang, H.; Zhu, C.; Niu, L.; Wang, X.; Fu, W.; Yu, P.; Chang, T. R.; Hsu, C. H.; Wu, D.; Jeng, H. T.; Huang, Y.; Lin, H.; Shen, Z.; Yang, C.; Lu, L.; Suenaga, K.; Zhou, W.; Pantelides, S. T.; Liu, G.; Liu, Z. Large-Area and High-Quality 2D Transition Metal Telluride. *Adv. Mater.* **2017**, *29* (3), 1603471.

(30) Chen, K.; Chen, Z.; Wan, X.; Zheng, Z.; Xie, F.; Chen, W.; Gui, X.; Chen, H.; Xie, W.; Xu, J. A Simple Method for Synthesis of High-Quality Millimeter-Scale 1T′ Transition-Metal Telluride and Near-Field Nanooptical Properties. *Adv. Mater.* **2017**, *29* (38), 1700704.

(31) Kim, T.; Park, H.; Joung, D.; Kim, D.; Lee, R.; Shin Chae, H.; Diware, M.; Chegal, W.; Jeong Soo, H.; Shin Jae, C.; Park, J.; Kang, S. W. Wafer-Scale Epitaxial 1T′, 1T′−2H Mixed, and 2H Phases MoTe$_2$ Thin Films Grown by Metal−Organic Chemical Vapor Deposition. *Adv. Mater. Interfaces* **2018**, *5*, 1800439.

(32) Park, J. C.; Yun, S. J.; Kim, H.; Park, J.-H.; Chae, S. H.; An, S.-J.; Kim, J.-G.; Kim, S. M.; Kim, K. K.; Lee, Y. H. Phase-Engineered Synthesis of Centimeter-Scale 1T′- and 2H-Molybdenum Ditelluride Thin Films. *ACS Nano* **2015**, *9* (6), 6548−6554.

(33) Zhou, L.; Xu, K.; Zubair, A.; Zhang, X.; Ouyang, F.; Palacios, T.; Dresselhaus Mildred, S.; Li, Y.; Kong, J. Role of Molecular Sieves in the CVD Synthesis of Large-Area 2D MoTe$_2$. *Adv. Funct. Mater.* **2017**, *27* (3), 1603491.

(34) Zhou, L.; Zubair, A.; Wang, Z.; Zhang, X.; Ouyang, F.; Xu, K.; Fang, W.; Ueno, K.; Li, J.; Palacios, T.; Kong, J.; Dresselhaus Mildred, S. Synthesis of High-Quality Large-Area Homogenous 1T′ MoTe$_2$ from Chemical Vapor Deposition. *Adv. Mater.* **2016**, *28* (43), 9526−9531.

(35) Yang, L.; Zhang, W.; Li, J.; Cheng, S.; Xie, Z.; Chang, H. Tellurization Velocity-Dependent Metallic−Semiconducting−Metallic Phase Evolution in Chemical Vapor Deposition Growth of Large-Area, Few-Layer MoTe$_2$. *ACS Nano* **2017**, *11* (2), 1964−1972.

(36) Gatensby, R.; McEvoy, N.; Lee, K.; Hallam, T.; Berner, N. C.; Rezvani, E.; Winters, S.; O'Brien, M.; Duesberg, G. S. Controlled synthesis of transition metal dichalcogenide thin films for electronic applications. *Appl. Surf. Sci.* **2014**, *297*, 139−146.

(37) Laskar, M. R.; Ma, L.; Kannappan, S.; Sung Park, P.; Krishnamoorthy, S.; Nath, D. N.; Lu, W.; Wu, Y.; Rajan, S. Large area single crystal (0001) oriented MoS$_2$. *Appl. Phys. Lett.* **2013**, *102* (25), 252108.

(38) Li, G.; Zhang, D.; Qiao, Q.; Yu, Y.; Peterson, D.; Zafar, A.; Kumar, R.; Curtarolo, S.; Hunte, F.; Shannon, S.; Zhu, Y.; Yang, W.; Cao, L. All The Catalytic Active Sites of MoS$_2$ for Hydrogen Evolution. *J. Am. Chem. Soc.* **2016**, *138* (51), 16632−16638.

(39) Seh, Z. W.; Kibsgaard, J.; Dickens, C. F.; Chorkendorff, I.; Nørskov, J. K.; Jaramillo, T. F. Combining theory and experiment in electrocatalysis: Insights into materials design. *Science* **2017**, *355* (6321), eaad4998.

(40) Tang, Q.; Jiang, D.-e. Mechanism of Hydrogen Evolution Reaction on 1T-MoS$_2$ from First Principles. *ACS Catal.* **2016**, *6* (8), 4953−4961.

(41) Eftekhari, A. Molybdenum diselenide (MoSe$_2$) for energy storage, catalysis, and optoelectronics. *Applied Materials Today* **2017**, *8*, 1−17.

(42) Gholamvand, Z.; McAteer, D.; Backes, C.; McEvoy, N.; Harvey, A.; Berner, N. C.; Hanlon, D.; Bradley, C.; Godwin, I.; Rovetta, A.; Lyons, M. E. G.; Duesberg, G. S.; Coleman, J. N. Comparison of liquid exfoliated transition metal dichalcogenides reveals MoSe$_2$ to be the most effective hydrogen evolution catalyst. *Nanoscale* **2016**, *8* (10), 5737−5749.

(43) Kong, D.; Wang, H.; Cha, J. J.; Pasta, M.; Koski, K. J.; Yao, J.; Cui, Y. Synthesis of MoS$_2$ and MoSe$_2$ Films with Vertically Aligned Layers. *Nano Lett.* **2013**, *13* (3), 1341−1347.

(44) Benck, J. D.; Hellstern, T. R.; Kibsgaard, J.; Chakthranont, P.; Jaramillo, T. F. Catalyzing the Hydrogen Evolution Reaction (HER) with Molybdenum Sulfide Nanomaterials. *ACS Catal.* **2014**, *4* (11), 3957−3971.

(45) McGlynn, J. C.; Cascallana-Matías, I.; Fraser, J. P.; Roger, I.; McAllister, J.; Miras, H. N.; Symes, M. D.; Ganin, A. Y. Molybdenum Ditelluride Rendered into an Efficient and Stable Electrocatalyst for the Hydrogen Evolution Reaction by Polymorphic Control. *Energy Technology* **2018**, *6* (2), 345−350.

(46) Eftekhari, A. Tungsten dichalcogenides (WS$_2$, WSe$_2$, and WTe$_2$): materials chemistry and applications. *J. Mater. Chem. A* **2017**, *5* (35), 18299−18325.

(47) Li, J.; Hong, M.; Sun, L.; Zhang, W.; Shu, H.; Chang, H. Enhanced Electrocatalytic Hydrogen Evolution from Large-Scale, Facile-Prepared, Highly Crystalline WTe$_2$ Nanoribbons with Weyl Semimetallic Phase. *ACS Appl. Mater. Interfaces* **2018**, *10* (1), 458−467.

(48) Richoux, V.; Diliberto, S.; Boulanger, C.; Lecuire, J. M. Pulsed electrodeposition of bismuth telluride films: Influence of pulse parameters over nucleation and morphology. *Electrochim. Acta* **2007**, *52* (9), 3053−3060.

(49) McEvoy, N.; Peltekis, N.; Kumar, S.; Rezvani, E.; Nolan, H.; Keeley, G. P.; Blau, W. J.; Duesberg, G. S. Synthesis and analysis of thin conducting pyrolytic carbon films. *Carbon* **2012**, *50* (3), 1216−1226.

(50) Ma, X.; Guo, P.; Yi, C.; Yu, Q.; Zhang, A.; Ji, J.; Tian, Y.; Jin, F.; Wang, Y.; Liu, K.; Xia, T.; Shi, Y.; Zhang, Q. Raman scattering in the transition-metal dichalcogenides of 1T′ MoTe$_2$ and T$_d$ WTe$_2$. *Phys. Rev. B: Condens. Matter Mater. Phys.* **2016**, *94* (21), 214105.

(51) Song, Q.; Wang, H.; Pan, X.; Xu, X.; Wang, Y.; Li, Y.; Song, F.; Wan, X.; Ye, Y.; Dai, L. Anomalous in-plane anisotropic Raman response of monoclinic semimetal 1 T′-MoTe$_2$. *Sci. Rep.* **2017**, *7* (1), 1758.

(52) Yoo, Y.; DeGregorio, Z. P.; Su, Y.; Koester, S. J.; Johns, J. E. In-Plane 2H-1T′ MoTe2 Homojunctions Synthesized by Flux-Controlled Phase Engineering. *Adv. Mater.* **2017**, *29* (16), 1605461.

(53) Camacho-López, M. A.; Escobar-Alarcón, L.; Picquart, M.; Arroyo, R.; Córdoba, G.; Haro-Poniatowski, E. Micro-Raman study of the m-MoO$_2$ to α-MoO$_3$ transformation induced by cw-laser irradiation. *Opt. Mater.* **2011**, *33* (3), 480−484.

(54) Mirabelli, G.; McGeough, C.; Schmidt, M.; McCarthy, E. K.; Monaghan, S.; Povey, I. M.; McCarthy, M.; Gity, F.; Nagle, R.; Hughes, G.; Cafolla, A.; Hurley, P. K.; Duffy, R. Air sensitivity of MoS$_2$, MoSe$_2$, MoTe$_2$, HfS$_2$, and HfSe$_2$. *J. Appl. Phys.* **2016**, *120* (12), 125102.

(55) Ye, F.; Lee, J.; Hu, J.; Mao, Z.; Wei, J.; Feng, P. X. L. Environmental Instability and Degradation of Single- and Few-Layer WTe$_2$ Nanosheets in Ambient Conditions. *Small* **2016**, *12* (42), 5802−5808.

(56) Roy, A.; Movva, H. C. P.; Satpati, B.; Kim, K.; Dey, R.; Rai, A.; Pramanik, T.; Guchhait, S.; Tutuc, E.; Banerjee, S. K. Structural and Electrical Properties of MoTe$_2$ and MoSe$_2$ Grown by Molecular Beam Epitaxy. *ACS Appl. Mater. Interfaces* **2016**, *8* (11), 7396−7402.

(57) Zhan, Y.; Liu, Z.; Najmaei, S.; Ajayan, P. M.; Lou, J. Large-Area Vapor-Phase Growth and Characterization of MoS2 Atomic Layers on a SiO2 Substrate. *Small* **2012**, *8* (7), 966−971.

(58) Trentler, T. J.; Hickman, K. M.; Goel, S. C.; Viano, A. M.; Gibbons, P. C.; Buhro, W. E. Solution-Liquid-Solid Growth of Crystalline III-V Semiconductors: An Analogy to Vapor-Liquid-Solid Growth. *Science* **1995**, *270* (5243), 1791−1794.

(59) Kwak, J.; Jo, Y.; Song, S.; Kim, J. H.; Kim, S.-Y.; Lee, J.-U.; Lee, S.; Park, J.; Kim, K.; Lee, G.-D.; Yoo, J.-W.; Kim, S. Y.; Kong, Y.-M.; Lee, G.-H.; Lee, W.-G.; Park, J.; Xu, X.; Cheong, H.; Yoon, E.; Lee, Z.; Kwon, S.-Y. Single-Crystalline Nanobelts Composed of Transition Metal Ditellurides. *Adv. Mater.* **2018**, *30* (30), 1707260.

(60) Chhowalla, M.; Shin, H. S.; Eda, G.; Li, L.-J.; Loh, K. P.; Zhang, H. The chemistry of two-dimensional layered transition metal dichalcogenide nanosheets. *Nat. Chem.* **2013**, *5*, 263.

(61) Chia, X.; Eng, A. Y. S.; Ambrosi, A.; Tan, S. M.; Pumera, M. Electrochemistry of Nanostructured Layered Transition-Metal Dichalcogenides. *Chem. Rev.* **2015**, *115* (21), 11941−11966.

(62) Voiry, D.; Salehi, M.; Silva, R.; Fujita, T.; Chen, M.; Asefa, T.; Shenoy, V. B.; Eda, G.; Chhowalla, M. Conducting MoS$_2$ Nanosheets as Catalysts for Hydrogen Evolution Reaction. *Nano Lett.* **2013**, *13* (12), 6222−6227.

(63) Tsai, C.; Chan, K.; Nørskov, J. K.; Abild-Pedersen, F. Theoretical insights into the hydrogen evolution activity of layered transition metal dichalcogenides. *Surf. Sci.* **2015**, *640*, 133−140.

(64) Xie, J.; Zhang, H.; Li, S.; Wang, R.; Sun, X.; Zhou, M.; Zhou, J.; Lou, X. W.; Xie, Y. Defect-Rich MoS$_2$ Ultrathin Nanosheets with Additional Active Edge Sites for Enhanced Electrocatalytic Hydrogen Evolution. *Adv. Mater.* **2013**, *25* (40), 5807−5813.

(65) McAteer, D.; Gholamvand, Z.; McEvoy, N.; Harvey, A.; O'Malley, E.; Duesberg, G. S.; Coleman, J. N. Thickness Dependence and Percolation Scaling of Hydrogen Production Rate in MoS$_2$ Nanosheet and Nanosheet−Carbon Nanotube Composite Catalytic Electrodes. *ACS Nano* **2016**, *10* (1), 672−683.

(66) Nolan, H.; McEvoy, N.; O'Brien, M.; Berner, N. C.; Yim, C.; Hallam, T.; McDonald, A. R.; Duesberg, G. S. Molybdenum disulfide/pyrolytic carbon hybrid electrodes for scalable hydrogen evolution. *Nanoscale* **2014**, *6* (14), 8185−8191.

(67) Kosmala, T.; Coy Diaz, H.; Komsa, H. P.; Ma, Y.; Krasheninnikov, A. V.; Batzill, M.; Agnoli, S. Metallic Twin Boundaries Boost the Hydrogen Evolution Reaction on the Basal Plane of Molybdenum Selenotellurides. *Adv. Energy Mater.* **2018**, *8*, 1800031.

(68) Shinagawa, T.; Garcia-Esparza, A. T.; Takanabe, K. Insight on Tafel slopes from a microkinetic analysis of aqueous electrocatalysis for energy conversion. *Sci. Rep.* **2015**, *5*, 13801.

(69) Seok, J.; Jun-Ho, L.; Suyeon, C.; Byungdo, J.; Hyo Won, K.; Min, K.; Dohyun, K.; Young-Min, K.; Sang Ho, O.; Sung Wng, K.; Young Hee, L.; Young-Woo, S.; Heejun, Y. Active hydrogen evolution

through lattice distortion in metallic MoTe$_2$. *2D Mater.* **2017**, *4* (2), 025061.